Influence of the Slant Angle of 3D Bluff Bodies on Longitudinal Vortex Formation

Patrick Gilliéron*, Annie Leroy[+], Sandrine Aubrun[+], Pierre Audier[+]

*"*Fluid Dynamics & Aerodynamics*" *Team, Research Department, Renault SA*
Service 68260, code API: TCR AVA 058
1, Avenue du Golf,
78288 Guyancourt Cedex
Phone : +33 1 76 85 70 40 / Fax : +33 1 76 86 91 18
patrick.gillieron@renault.com

[+] *Institut PRISME*
8 rue Leonard de Vinci
F-45072 Orleans cedex 2
Phone : +33 2 38 49 24 59 / Fax: +33 2 38 41 73 83
annie.leroy@univ-orleans.fr

Corresponding author : annie.leroy@univ-orleans.fr

Abstract:

This paper presents experimental results and analytical arguments concerning simplified geometries of the rear window and windscreen of automotive vehicles in order to contribute to a better understanding of the swirling structure formation and vortex bursting processes. Static pressure distributions and skin friction line visualisations on both sides of the edge where the swirling structure is generated on the rear window of an Ahmed body are presented for different slant angles. Results show the influence of the slant angle on the swirling structure formation and further show that the vortex bursting process can be promoted by small rear window angles. These results are then extrapolated with the help of analytical demonstrations to the windscreen configuration to demonstrate that large windscreen slopes would have the same disintegration effect.

Key words: Slant-Angle of Bluff Bodies / Vortex breakdown / Longitudinal vortices / Swirl Number

1 Introduction

The study of longitudinal swirling separated structures is of great interest in reducing the advance resistance of ground and air vehicles. In automobile aerodynamics, these structures account for close to 15% of resistance [1] and their suppression could reduce carbon dioxide emissions by 6 grams per kilometer (according to the New European Driving Cycle [2]). From a geometrical point of view, these structures can be eliminated by increasing the local radius of curvature from the side edges of the windscreen and rear window. However, this solution would have a strong impact on the vehicles' capacity and design, which cannot be considered at the present time. Work is therefore in progress to analyze and control the development of these structures and limit their impact on aerodynamic drag without constraining the automobile geometries.

Blowing and aspiration solutions are being developed on simplified geometries to burst, reduce or increase the radial development of the longitudinal swirling structures of the windscreen and rear window. For the rear window, a reduction of 6% [3,4] in aerodynamic drag is possible thanks to blowing when the swirl number, here defined as the maximum value of the ratio of the azimuthal velocity V_θ (rotational motion) to the longitudinal velocity V_X (advection motion), in a system coordinate linked to the swirling structure, is close to 1.5 [5,6]. For the windscreen, aspiration of the swirling structures provides reductions close to 5% [7]. Others definitions of the swirl number have been introduced in the past. Each definition is associated with a distinct vortex breakdown criterion. Rusak et al. [8] proposed a definition of the swirl number in accordance with a theory on the axisymmetric vortex breakdown process, which is applied to vortices in pipes and above slender wings in order to exhibit a criterion for the appearance of breakdown [9]. In this paper focusing on vortices around simplified automobile geometries, the above definition is retained for the swirl number allowing a direct comparison with some results on the features and breakdown of such vortices [3,4,6,7].

Analysis of the longitudinal velocity field of these structures clearly shows differences between the structures of the windscreen and those of the rear window [6,7]. When bursting or swirl

destructuring are not forced, the transverse fields of the axial velocities are respectively wake-like [7] and jet-like [6]. Improving the energy efficiency of the control requires a better knowledge of the origin of these differences.

This paper proposes a contribution to the analysis of the physical mechanisms responsible for these structural differences by focusing on the influence of the slant angle of the windscreen and rear window. Analytical considerations and experimental results concerning pressure distributions and skin friction lines are used to study the influence of different geometrical factors on the formation and swirling processes.

2 Field of Analysis

The analysis of longitudinal swirling separated structures is carried out thanks to the results obtained on simplified geometries of plane windscreens and rear windows, which make a slant angle of θ with regards to the upstream flow direction V_0 (Figs. 1 and 2). As in most previous studies for windscreen flow and rear window flow, a dihedral bluff body [7] and an Ahmed body [10], as described in Fig.1 and Fig. 2, are respectively investigated.

Flow separations are observed on the left and right sides of the windscreen. They are responsible for the appearance of two main contrarotating longitudinal swirling structures [7] (Fig. 3). As regards the rear window, flow detachments are observed on the top and on the left and right sides to form and feed a detachment sheet D, two main contrarotating longitudinal swirling structures A and two contrarotating swirling structures B centered on two separation foci [11] (Fig. 4). The source of the swirling structures on the top is the upstream flow and the left and right side flows which move up towards the end of the roof before the separation line [12]. It is well known that each principal longitudinal swirling structure creates a secondary longitudinal swirling structure, which can be clearly discerned on wall visualizations (Figs. 3 and 4). The topology of the flow on the rear window is similar to an Ahmed body [10-15] for slant angles of rear window ranging between 12 and 30 degrees (Fig. 4).

The nature of these longitudinal swirling structures differs depending on the attachment line direction. When bursting or swirl destructuring are not forced, the axial velocity profiles of a transverse velocity field are wake-like [7] and jet-like [6] for the windscreen and rear window respectively.

On the rear window in a left rear view, the vortex emanates from the y=0 line and evolves in the y>0 plane (Fig. 5). As the attachment line is windward, the velocity vector $\vec{W}$, resulting from the composition of the azimuthal velocity V_θ and the freestream velocity V_0, is convergent in direction towards the longitudinal vortex axis, continuously increasing the axial flow rate. Hence,

the local axial velocity profile evolves to a jet-like velocity profile according to the continuity equation as shown in Fig. 6.

On the lateral edge of the windscreen, the attachment line is leeward. The azimuthal velocity decreases as the distance from the vortex core top increases. Consequently, this resulting velocity vector $\vec{W}$ (Fig. 7) diverges in direction from the longitudinal vortex axis, decreasing the axial flow rate contrary to the rear window. Hence, the local axial velocity profile evolves to a wake-like velocity profile according to the continuity equation as shown in Fig. 6.

Experiments focusing on these separated longitudinal swirling structures around simplified rear window or windscreen geometries [6-7] confirm this observation.

In the following sections, the results of experiments performed on an Ahmed body and analytical considerations are used to study the influence of different factors such as slant angle values and pressure gradient distributions on the formation processes and on the flow topology.

3 Experimental Set-up

Tests were run in the Lucien Malavard wind tunnel at the PRISME Institute. It is a closed-circuit wind tunnel with a square 2 m x 2 m section 5 m in length. The maximum inflow velocity is 60 $m.s^{-1}$ with differences of less than 1 % of the mean value in the effective test section and with a turbulence level of 0.4 %. For the present experiments, the reference velocity was V_0 = 30 $m.s^{-1}$, leading to a Reynolds number based on the length of the model L of 2.10^6.

The Ahmed body at a scale of 1:1 is made of PVC and its dimensions are L = 1.044 m long, l = 0.389 m wide and H = 0.288 m high, see Fig. 2. Several configurations of slant angle were designed and tested: θ = 15°, 20° for 25° (the slanted edge length is uniform l_w = 0.222 m). The model was fixed in the centre of the test section, on a 3 m long plate, with four feet each 0.030 m in diameter and 0.1 m in height. The blockage ratio is about 3%.

The model was equipped with 43 pressure taps located on the slanted edge and on one side of it along the lines D_1, D_2, D_3, D_4 and D_L (Figs. 8 and 9). The lines D_1, D_2, D_3, D_4 are located on

the side of the rear window and meet the point P (coordinates x = 0, y = 0, z = 0). D_1 is vertical. The lines D_2 and D_3 are uniformly evenly spaced between D_1 and D_4. The line D_4 is parallel to the edge between the rear window and the rear window side and is located 0.005 m from it. The line D_L is parallel to the edge between the rear window and the rear window side and is located, on the rear window, 0.005 m from it (Fig. 9).

The pressure taps were connected by a 0.15 m long plastic tubing to 43 PSI pressure transducers (ESP-32HD and ESP-16HD). The precision of the pressure transducers is +/- 0.1 % of the full scale for the ESP-32HD and +/- 0.06 % of the full scale for the ESP-16HD. Each of the pressure transducer inputs was scanned at 200 Hz during 10.25 seconds.

The pressure is given in the usual form of the pressure coefficient $Cp = \frac{p - p_0}{0.5\rho V_0^2}$, where p_0 and V_0 are the freestream static pressure and velocity, respectively, far upstream of the model. The static pressure distributions enable the influence of the slant angle on the wall signature of the longitudinal swirling structures to be quantified since it is well known that the more the slant angle increases, the stronger the longitudinal swirling structures will become.

Friction line visualisations on the slanted edge and on its side were performed using a viscous coating made of oleic acid, dodecane, silicon oil and titanium dioxide [16]. The wall was coated with the mixture using a brush. The model was then exposed to a constant wind until the friction lines became visible. These visualisations make it possible to study the influence of the slant angle on the friction line directions upstream of the geometrical discontinuities between the side of the main body and the rear window.

No similar experimental results on the windscreen configuration are available in the present paper.

4 Influence of Geometrical Discontinuities on Static Pressure Coefficient Distributions

Longitudinal swirling structures result from a complex interaction mechanism between adjacent and convergent flows around geometrical discontinuities of convex surfaces. These discontinuities influence static pressure coefficient distributions and consequently vortex formation.

For the rear window, the longitudinal vortices result from convergence of the Ahmed body roof flow and the two lateral side flows. According to the Euler equations in the transverse flow direction, and because of the geometrical discontinuities which create a sharp spreading associated with a reduction in radius of curvature, the flow is accelerated and static pressure coefficient values are the lowest on the top and side of the rear window, as mentioned in [15] and shown in Fig. 11. It is well established that this zone of highest depression is observed just behind the top edge of the rear window. This feature can also be deduced from an analytical point of view. Following a friction line along the roof and the rear window, the static pressure diminishes because of the reduction in the radius of curvature according to the Euler equations. If S_{up} and S_{down} are parallel sections of the same streamtube perpendicular to the geometry surfaces and if V_{up} is the air flow velocity in the boundary layer upstream of the end of the roof, as shown in Fig. 10, the total pressure (or volume energy) loss ΔP_i associated with the sharp spreading is given by:

$$\Delta P_i = \left(1 - \frac{S_{up}}{S_{down}}\right)^2 \frac{\rho}{2} V_{up}^2 \text{ with } S_{down} = S_{up}(1+\varepsilon) \text{ and } \varepsilon \to 0 \quad (1)$$

As ΔP_i tends to locally vanish, local velocities and static pressure coefficients are linked by the equation:

$$C_P^{down} - C_P^{up} = 1 - \left(\frac{V_{down}}{V_{up}}\right)^2 \quad (2)$$

The flow can be considered as a flow along a flat plane a without longitudinal pressure gradient, and therefore:

$$(\frac{V_{down}}{V_{up}})^2 \approx 1 - C_P^{down} > 1 \quad (3)$$

and V_{down} is higher than V_{up}. The lowest value of the static pressure coefficient C_P^{down} is therefore observed in the upper part of the rear window.

Fig. 11 shows the static pressure coefficient distributions on the lateral side of the rear window and on the rear window for different slant angles. It is noticeable that the static pressure gradients increase on the lateral side and at the edge of the rear window, close to P, as the slant angle increases. This engenders the formation of a vortex structure and amplification of swirling. Furthermore, the signature of the longitudinal swirling structures, characterised by an additional static pressure loss below them, is more and more visible on the rear window.

In the case of the windscreen, the longitudinal vortices result from convergence of the lateral and transverse flows on the windscreen. When the slant angle θ increases, two main phenomena contribute to make higher underpressure apparent [6]. Firstly it is well established that a positive Cp zone is observable in the central region of the base of the windscreen, and that its size increases with the slant angle. Secondly the normal component of the upstream velocity (Fig. 12) increases as the angular deviation λ increases, hence the static pressure coefficient near the junction edge decreases. The consequence of these two phenomena is an increase in the pressure gradient in the direction of the friction lines, which causes an increase in local velocities near the top and lateral part of the windscreen. Associated with this velocity increase is a reduction in the peripheral static pressure coefficients that enlarges proximal areas with a weak radius of curvature.

Beyond a deviation angle of 90°, the axial component of the shedding velocity near the lateral geometrical discontinuities vanishes and the three-dimensional nature of the detachment mechanism becomes a bi-dimensional problem (the case of the windscreen or completely vertical rear part perpendicular to the freestream velocity).

Finally, the lowest values of static pressure coefficient and the highest values of velocities are observed at downstream junction lines between the roof and the rear window, between the vertical lateral sides and the rear window, and between the windscreen and lateral windows. When the slant angle increases, higher underpressure can be observed. This engenders the vortex structure formation and amplification of swirling.

5 Influence of the Radial and Transverse Pressure Gradients

The static pressure coefficient distributions are shown in a different manner in Figs 13 and 15. They can be used to assess, with the finite difference method, the static pressure gradients along the radial directions centred on P $\left.\frac{\partial Cp}{\partial r}\right|_{D_1}$, $\left.\frac{\partial Cp}{\partial r}\right|_{D_2}$, $\left.\frac{\partial Cp}{\partial r}\right|_{D_3}$ and $\left.\frac{\partial Cp}{\partial r}\right|_{D_4}$ (Fig. 14), and the difference of static pressure coefficients across the edge between the side of the body and the rear window $\Delta Cp = Cp|_{D_4} - Cp|_{D_L}$ (Fig. 16).

The static pressure coefficient on the side of the rear window continuously increases along the four line D_i (i = 1 to 4), when the radius increases and/or when the slant angle decreases (Fig. 13), except for the line D_4 at θ = 20° and 25°. An inversion of trend is visible close to the point P when the slant angle increases. A spot of higher pressure appears at $\frac{r}{l} = 0.07$ on D_4 for θ = 25°. The θ = 20° case seems to be a transition case between the two trends since it presents some non-interpretable oscillations [3]. The most noticeable flow modification when the slant angle increases is the progressive formation of a streamwise swirling structure on both sides of the Ahmed body, with a centreline origin merged with the point P. It is then logical to try to link the appearance of this spot of relatively high pressure close to P when θ increases with the formation mechanism of the streamwise swirling structures.

The static pressure coefficients measured on the rear window along the line D_L are shown in

Fig. 15. For the three slant angles, the static pressure coefficients increase with the reduced abscissa, except for the measurement location closest to P, in x/l=0.07. This local spot of relatively higher pressure close to P suggests the existence of attachment nodes on the upper corners of the rear window. [11-12] showed that the influence of these nodes on the local topology increases with the slant angle.

The static pressure coefficients measured on the rear window are compared in Fig. 15 with the static pressure coefficients measured on the side of the body, along the line D_4. The difference between these coefficients $\Delta Cp = Cp\big|_{D_4} - Cp\big|_{D_L}$ when the distance from P increases is plotted in Fig. 16. The difference is in all cases positive and increases with the slant angle, illustrating the local suction effect on the rear window responsible for the distortion of streamlines coming from the side part of the body and attracted to the rear window, thus leading to the swirling structure formation. The static pressure coefficient difference is particularly high for the locations closest to P. This tendency was also visible on the static pressure coefficient gradient calculated along the radii on the rear window side (Fig.14). Smaller pressure coefficients are measured close to P on the lateral part but also on the rear window.

The present results show that the static pressure coefficients decrease and that the radial gradients of the static pressure and transverse differences of static pressure increase, as the distance from P decreases (except for the very local influence of the attachment nodes which tend to locally raise the pressure close to P). The point P, the apex of the swirling cone, could then be considered as the curvature centre of the local flow. In these conditions, the acceleration is centripetal, the motion is characterised by a central force, the kinetic momentum is constant and the tangential velocity, along a circle centred on P, decreases as the distance from P increases.

The influence of radial acceleration on the lateral flow trajectory which feeds the swirling structures is studied. Figs 17 and 18 show the angular deviation λ and the ratio between the angular deviation and the slant angle λ/θ, respectively, versus the distance from P for θ = 15°, 20° and 25°.

The angular deviation λ is measured on the friction line visualisations made with viscous coating on the side of the rear window, for slant angles θ = 15°, 20° and 25° (Figs. 19).

Globally, as the distance from P increases, the centripetal acceleration of the central force motion decreases, the flow trajectory moves away from the curvature centre P and the angular deviation decreases as shown in Fig. 17, where the linear regression curves clearly exhibit this evolution. In addition the plots show that the angular deviation λ decreases continuously for the smallest slant angle whereas it remains nearly constant until $x/l = 0.6$ for the largest slant angle. The middle configuration shows an intermediate tendency. This proves that the spatial domain along the lateral edge axis *x,* where the central acceleration acts, increases with the slant angle. However, the angular sector of the lateral side of the rear window (90° - θ) where the central acceleration acts, decreases as the slant angle increases. One would therefore expect the magnitude of the central acceleration to be lower and the angular deviation to be smaller for large slant angles. However, this feature is only visible very close to the point P, where λ is higher for smaller slant angles. Fig. 18 shows that the angular deviation growth rate is globally higher for smaller slant angles and is maximum close to P. This result tends to confirm again that the central acceleration acts the most for smaller slant angles. To summarize, the magnitude of the central acceleration decreases but the area over which it acts increases as the slant angle increases. These results will be used in the following section to establish that the swirl number increases as the slant angle decreases.

6 Slant Angle Influence on the Swirl Number

A phenomenon of special importance to swirling flows is vortex breakdown [4-5]. It can be beneficial in automotive applications where drag reduction is a goal. It is established that the maximum of ratio of the swirling (azimuthal) velocity V_θ to the longitudinal velocity V_X, is one of the most effective parameters to predict vortex breakdown. When the maximal value of this ratio, called the swirl number, goes beyond a critical value close to 1.5, then vortex breakdown will occur.

In this section, we analyze the influence of the slant angle on the swirl number defined here, in the (X,Y,Z) coordinate system linked to the swirling structure, as the maximum value of the ratio of the azimuthal velocity V_θ to the longitudinal velocity V_X, of the flow velocity vector V_λ emanating from the separation edge of the rear window. This velocity vector is projected on the symmetrical axis and in a normal plane to the swirling structure axis (Fig. 20). By noting α and β the precession and nutation angles respectively, its azimuthal and longitudinal components can be calculated as:

$$V_\theta = V_\lambda \left[\left[\sin\lambda\,\cos\alpha - \cos\lambda\,\sin\alpha\,\cos\beta\right]^2 + \cos^2\lambda\,\sin^2\beta\right]^{0.5} \quad (4)$$

$$V_X = V_\lambda \left[\sin\lambda\,\sin\alpha + \cos\lambda\cos\alpha\cos\beta\right] \quad (5)$$

The swirl number expression in relation with the deviation angle λ can be deduced from (4) and (5) considering small values of α and β close to 8 and 7 degrees [3-4] respectively:

$$S = \max \frac{V_\theta}{V_X} \approx \max(\tan\lambda) \quad (6)$$

Finally, the evolution of $\frac{V_\theta}{V_X}$ is shown in Fig. 21. This ratio increases as the deviation angle increases.

As shown in Fig. 17, higher values of the deviation angle λ, and consequently higher values of the swirl number, are observed around the top of the rear window edge for the smallest values of the slant angle. Hence, vortex breakdown may occur (a necessary but not a sufficient condition [4]) for low slant angles.

This result is then compared with numerical and experimental results from the literature. Vortex breakdown achieved for jet [3-4,17-18] and wake [7] swirling flows, confined or unconfined, occurs when the swirl number is close to 1.5. This value corresponds to a value of 64° for the deviation angle (Fig. 21).

According to the experimental results presented in the previous sections, the λ value

increases as the slant angle decreases, and the highest value is 70° for θ = 15° (Fig. 17). This value is greater than the theoretical value of 64 degrees (Fig. 21). This result here confirms the fact suggested by [5] that the condition is necessary but not sufficient. Moreover, it suggests that vortex breakdown or dramatic changes in vortex structures may occur for a slant angle lower than 15 degrees. According to [3], drag reduction is associated with this phenomenon. Drag measurements performed on an Ahmed body in references [10,11] have shown that for a slant angle of 12°, when these lateral longitudinal structures appear and grow, a drag increase is observed.

In the case of windscreen separation, by analogy with the results obtained for the rear window, the deviation angle λ, the azimuthal velocity and the swirl number are the highest when the slant angle of the windscreen is high and they diminish upwards from the bottom to the top of the windscreen edge. Hence, vortex breakdown may occur for high slant angles, as shown in [7], where numerical simulations of vortex breakdown were carried out for windscreen slant angles of 30 and 45 degrees.

7 Conclusion

Analytical approaches and experimental results on simplified geometries have made possible the analysis of the flow topology near the longitudinal swirling structures of a rear window and windscreen. End roof and windscreen geometrical discontinuities increase velocity and decrease the static pressures, which amplify the formation and rolling up processes of the swirling structures. For the rear window, parietal visualizations and static pressure cartographies at the top of the swirling cones show that a centripetal acceleration locally curves the flow trajectories before separation. The local flow is then subjected to a central force motion and the friction lines tend towards arcs of circle. Local velocities and angular deviations of the flow measured at the line of separation and projected onto the plane of the rear window or side plane, decrease as one moves away from the center of curvature.

The influence of the slant angle compared to the direction of the incident flow on the swirl

number value has been analyzed. The swirl number depends on the angular deviation of the incident flow compared to the separation line. Its value decreases and increases respectively when the slope of the rear window and windscreen increases. The bursting and swirl destructuring processes are promoted by small rear window angles and large windscreen slopes. The results obtained in experiments and/or numerically on simplified geometries of the rear window and windscreen confirm these results.

Nomenclature

V_o = freestream velocity

(x_0, y_0, z_0) = Coordinate system linked to the freestream velocity

(x, y, z) = Coordinate system linked to the left lateral edge (rear view)

(X, Y, Z) = Coordinate system linked to the swirling structure axis from the rear window

P = Intersection point between the left lateral edge (rear view) and the end of the roof

H = Ahmed body height

L = Ahmed body length

l = Ahmed body width

l_w = Rear window length

r = radius of curvature

S = Swirl number (the maximum value of the ratio of V_θ to V_X)

ΔP_i = Volume energy loss

S_{up} = Area normal to the freestream direction located upstream of the end of the roof

S_{down} = Area normal to the freestream direction located downstream of the end of the roof

V_{up} = Air flow velocity in the boundary layer upstream of the end of the roof

V_{down} = Air flow velocity in the boundary layer downstream of the end of the roof

C_P^{up} = Static pressure coefficient upstream of the end of the roof

C_P^{down} = Static pressure coefficient downstream of the end of the roof

$\vec{n}$ = Unit vector normal to the wall and directed towards the fluid domain

V_λ = Air flow velocity in the boundary layer at the lateral edge of the rear window

V_X = Longitudinal component of V_λ projected on X

V_θ = Azimuthal component of V_λ

Greek symbols:

ρ = Air density

θ = Slant angle

λ = Angle of the local velocity V_λ against the rear window

α = Swirling structure axis angle against the rear window

β = Swirling structure axis angle against the lateral side of the rear window

NEDC Cycle (for New European Driving Cycle) : certification cycle for all light vehicles in Europe.

References

[1.] Onorato, M., Costelli, A., and Garonne, A., 1984, "Drag Measurement Through Wake Analysis", SAE, SP-569, International Congress and Exposition, Detroit, Michigan, pp. 85-93.

[2.] Tzirakis, E., Pitsas, K., Zannikos, F., and Stournas, S., 2006, "Vehicle Emissions and Driving Cycles : Comparison of the Athens Driving Cycle (ADC) with ECE-15 and European Driving Cycle (EDC)", Global NEST Journal, **8**, n°3, pp. 282-290.

[3.] Lehugeur, B., Gilliéron, P., and Ivanic, T., 2006, "Contribution de l'Eclatement Tourbillonnaire à la Réduction de la Traînée des Véhicules Automobiles : Approche Numérique", Comptes Rendus de l'Académie des Sciences, **334**, pp. 368-372.

[4.] Lehugeur, B., and Gilliéron, P., 2006, "Active Control of Vortex Breakdown Phenomenon in the Wake of a Simplified Car Geometry", ASME Joint U.S. – European Fluids Engineering Summer Meeting, paper n° FEDSM2006-98349, Florida.

[5.] Billant, P., Chomaz, J.M., and Huerre P.,1998, "Experimental Study of Vortex Breakdown in Swirling Jets", J. Fluid Mech., **376**, pp. 183-219.

[6.] Lehugeur, B., Gilliéron, P., and Ta Phuoc, L., 2005, "Characterization of Longitudinal Vortices in the Wake of a Simplified Car Model", AIAA Paper No. 2005-5383.

[7.] Lehugeur, B., Gilliéron, P., and Ta-Phuoc, L., 2007, "Characterization and Control of Longitudinal Vortices Over a Dihedral Bluff Body: Numerical Approach", ASME J. Mech. Eng., **58**, 5.

[8.] Rusak, Z., Wang, S., and Whiting C. H., 1998, "The Evolution of a Perturbed Vortex in Pipe to Axisymmetric Vortex breakdown", J. Fluid. Mech., **366**, pp. 211-237.

[9.] Rusak, Z. and Lamb, D., 1999, "Prediction of Vortex Breakdown in Leading-Edge Vortices Above Slender Delta Wings", J. of Aircraft, **36**, pp. 659-667.

[10.] Ahmed, S., Ramm, R., and Falting, G., 1984, "Some Salient Features of the Time Averaged Ground Vehicle Wake", SAE Paper, No. 840300.

[11.] Gilliéron, P., and Chometon, F., 1999, "Modelling of Stationary Three-Dimensional Detached Airflows Around an Ahmed Reference Body", Int. Workshop on Vortex, ESAIM, **7**, 1999, pp. 183-182.

[12.] Spohn, A., and Gilliéron, P., 2002, "Flow Separations Generated by a Simplified Geometry of an Automotive Vehicle", IUTAM Symposium on Unsteady Separated Flows, France.

[13.] Krajnovic, S., and Davidson, L., 2004, "Contribution to Large-Eddy Simulation of the flow Around a Simplified Car Model", SAE Int. Congress & Exposition, SAE 2004-01-0227.

[14.] Rouméas, M., Gilliéron, P. and Kourta, A., 2008, "Separated Flow Around the Rear Window of a Simplified Car Geometry", ASME J. Fluids Eng., **130**, 021101-1.

[15.] Vino, G., Watkins, S., Mousley, P., Watmuff, J., and Prasad, S., 2005, "Flow Structures in the Near Wake of the Ahmed Model", J. Fluids and Struct., **20**, pp. 673-695.

[16.] Anne-Archard, D., Du Colombier, D., Boisson, H., and Herbert, V., 2006, "Analyse des Enduits de Visualisation Pariétale Utilisés en Aérodynamique", 41ème Colloque National du Groupe Français de Rhéologie, France.

[17.] Beran, P. S., and Culick, F. E. C., 1992, "The Role of Non Uniqueness in the Development of Vortex Breakdown in Tubes", J. Fluid Mech., **242**, pp. 491-527.

[18.] Carvalho, I. S., and Heitor, M. V., 1996, "Visualization of Vortex Breakdown in Turbulent Unconfined Jet Flows", Optical Diagnostics in Engineering, **1**, pp 22-30.

List of figures

Fig. 18 Ratio between the angular deviation and the slant angle versus the reduced distance from P, x/l, for slant angles θ = 15, 20 and 25°. Vo=30 m.s^{-1}

Fig. 19a Slant angle anḍ angular deviation of the lateral friction line λ

Fig. 19b Friction line visualisations on the side of the rear window. θ = 15°, Vo=30 m.s^{-1}

Fig. 19c Friction line visualisations on the side of the rear window. θ = 20°, Vo=30 m.s^{-1}

Fig. 19d Friction line visualisations on the side of the rear window. θ = 25°, Vo=30 m.s^{-1}

Fig. 20 Referential system linked to the swirling structure: Precession and nutation angles. Azimuthal V_θ and longitudinal V_X velocities in a X=Cte plane

Fig. 21 Evolution of the ratio of azimuthal V_θ and longitudinal V_X velocities as a function of the deviation angle λ

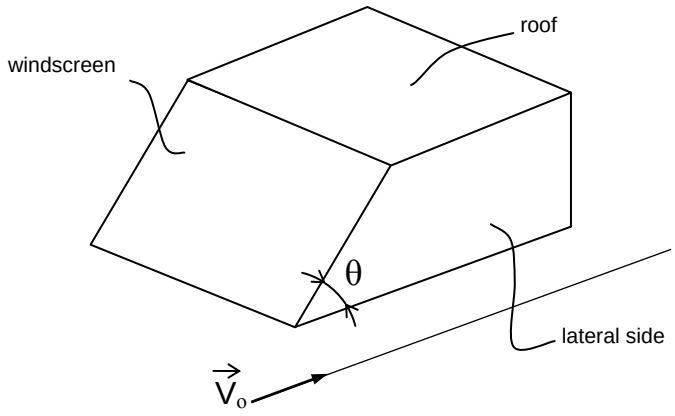

Fig. 1 Schematic representation of windscreen with a slant angle θ

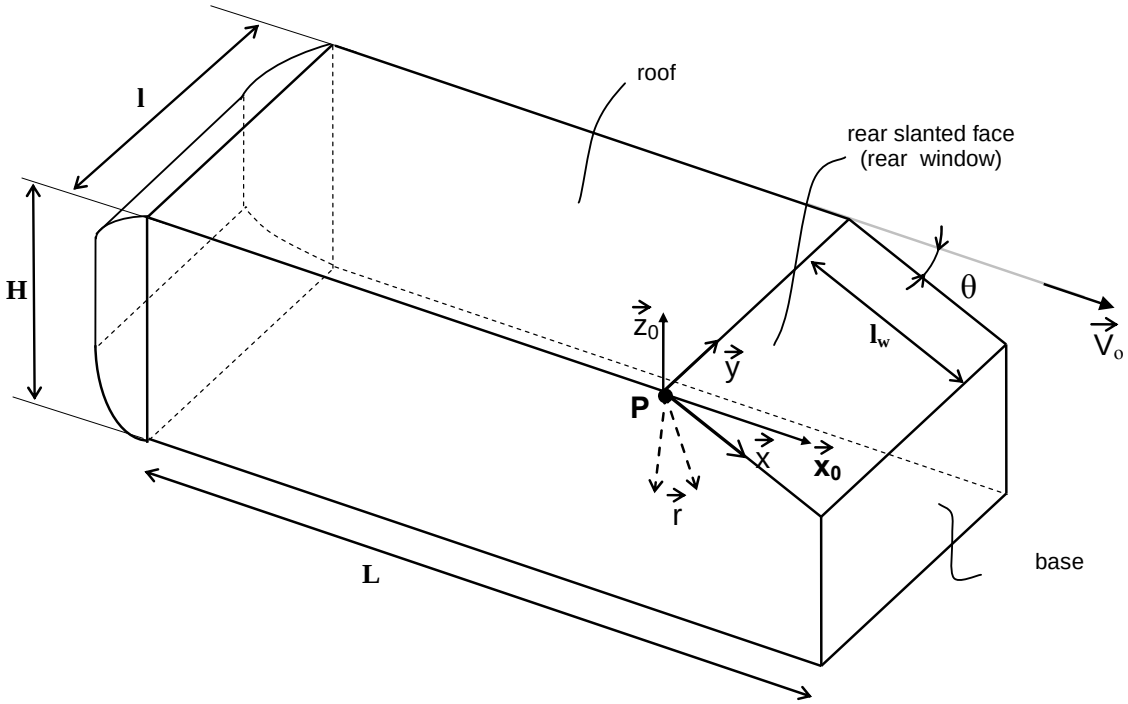

Fig. 2 Ahmed body geometry, from Ahmed et al [7], Slant angle θ of rear window.

(x_0, y_0, z_0) and (x, y, z) : frames linked to the freestream velocity direction and to the left side line of the rear window respectively

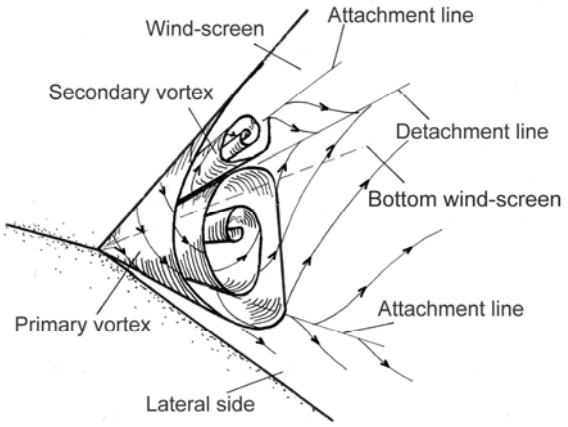

Fig. 3 Schematic representation of amount of the windscreen detachment, left back view ; the secondary structure is linked to the existence of the principal longitudinal swirling structure

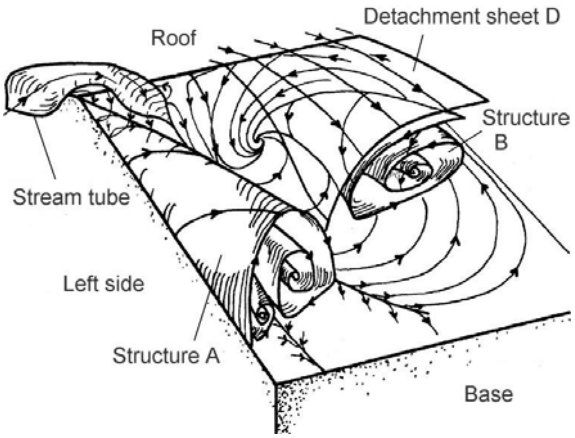

Fig. 4 Schematic representation of the left part of rear window detachment for slant angles θ ranging between 12 and 30 degrees, according to [7] & [9], back view

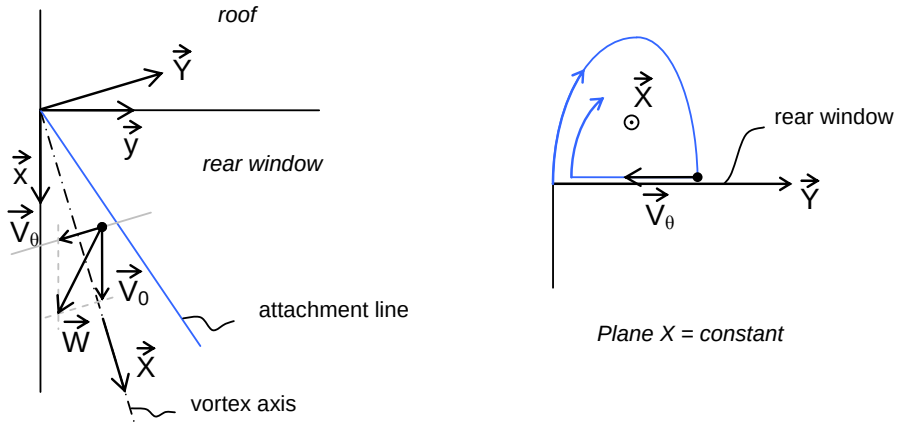

Fig. 5 Composition of azimuthal and freestream velocities V_θ and V_0 on the rear window, resulting velocity vector $\vec{W}$.

(X, Y, Z) : Coordinate system linked to the swirling structure axis

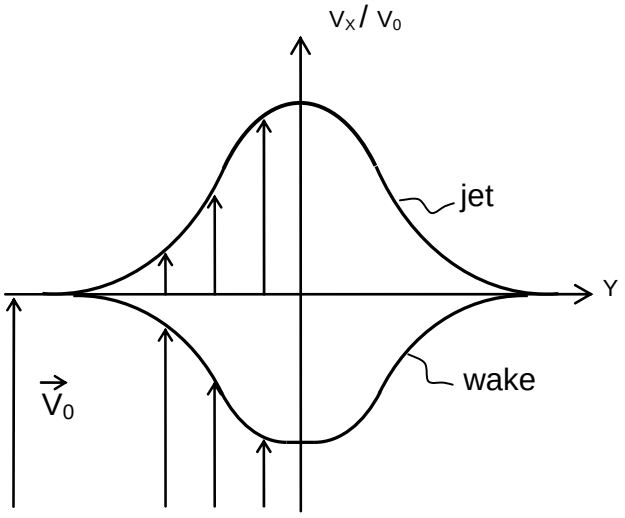

Fig. 6 Axial velocity profiles: jet and wake profiles

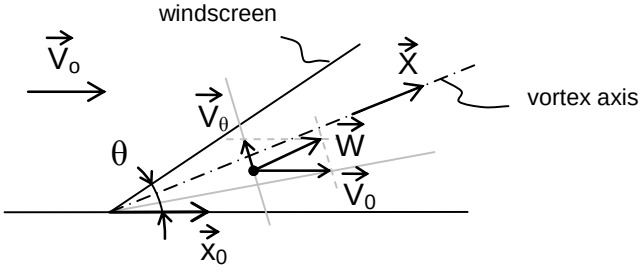

Fig. 7 Composition of azimuthal and freestream velocities V_θ and V_0 on the windscreen edge, resulting velocity vector $\vec{W}$

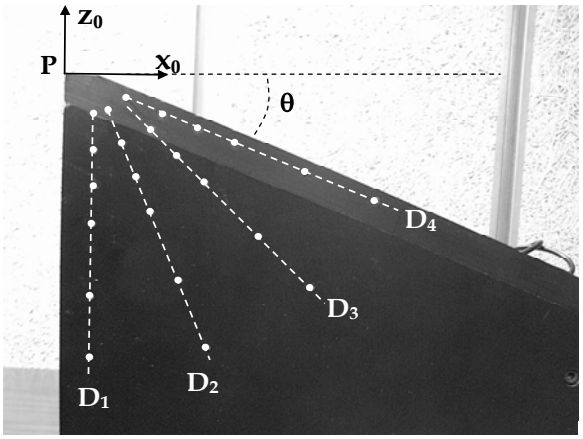

Fig. 8 Location of the static pressure tabs on the left side of the rear window. The four lines intersect at P

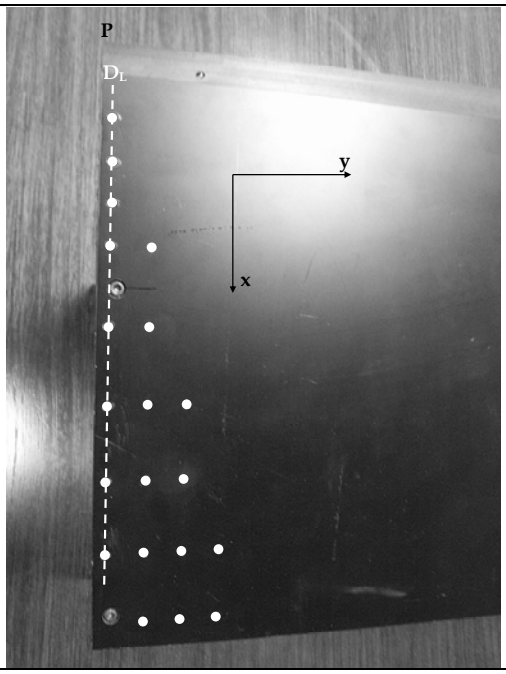

Fig. 9 Location of the static pressure tabs on the rear window

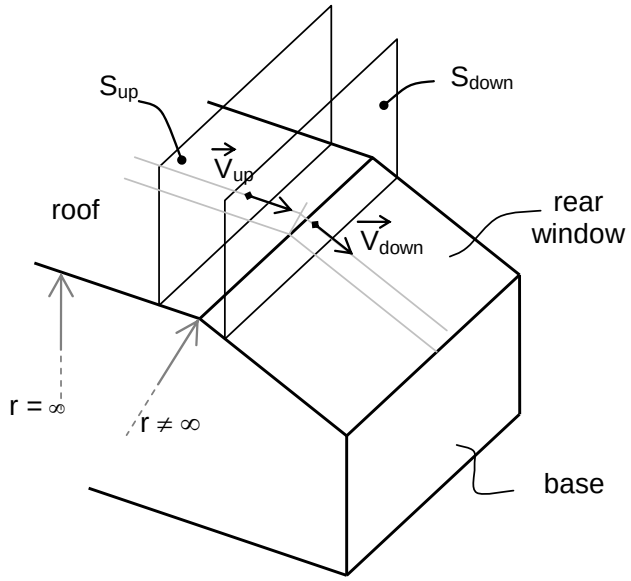

Fig. 10 Streamline representation along roof and rear window

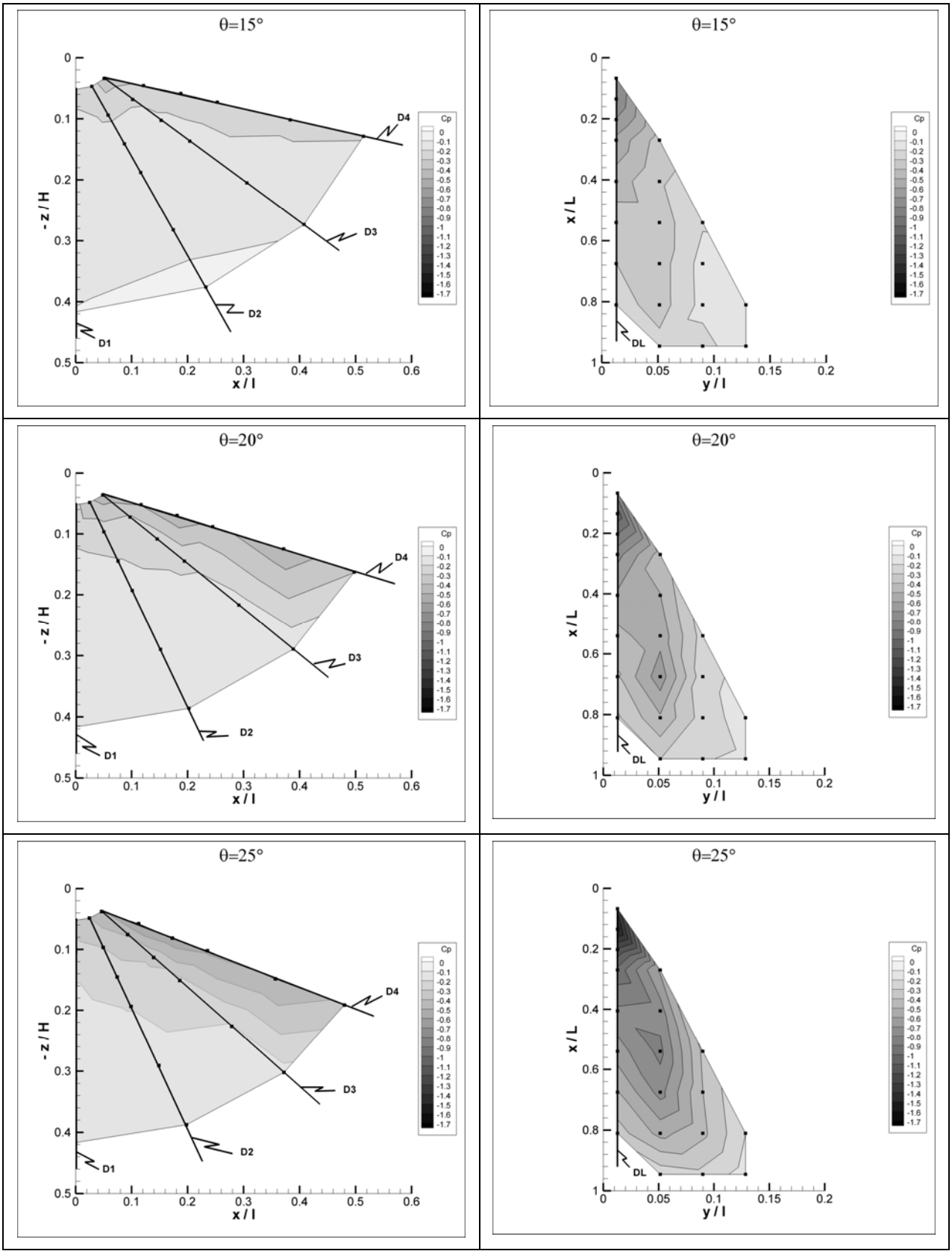

Fig. 11 Static pressure coefficient distribution on the side of the rear window (left) and on the rear window (right)

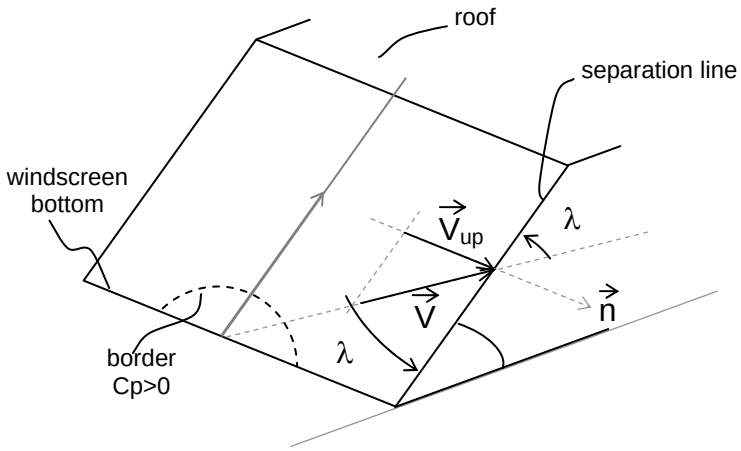

Fig. 12 Normal and tangential components of the flow velocity on the windscreen near the separation geometrical edge

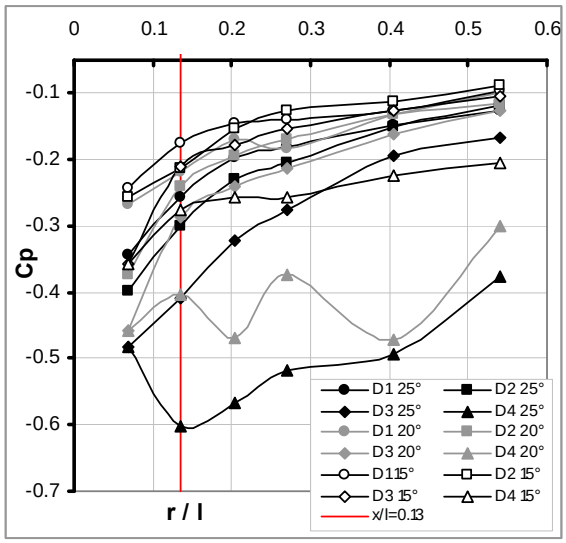

Fig. 13 Static pressure coefficients Cp along the lines D_1,D_2, D_3 and D_4 on the side of the rear window. Vo=30 m.s^{-1}

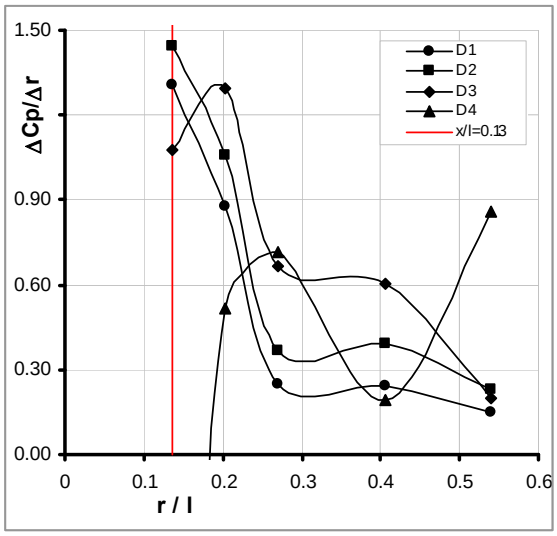

Fig. 14 Radial static pressure coefficient gradients along the lines D_1, D_2, D_3 and D_4. θ = 25°, Vo=30 m.s^{-1}

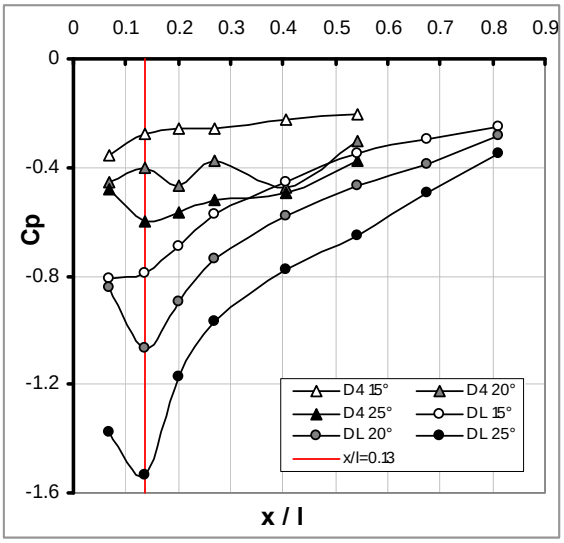

Fig. 15 Static pressure coefficients Cp along the lines D_L and D_4. Vo=30 m.s^{-1}

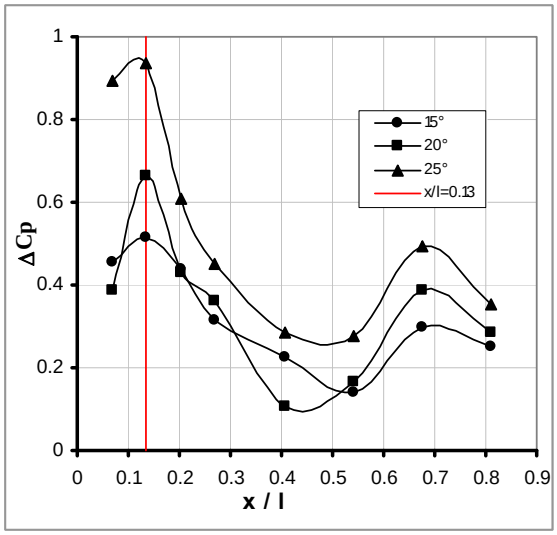

Fig. 16 Difference in static pressure coefficients along the lines D_4 and D_L: $\Delta Cp = Cp\big|_{D_4} - Cp\big|_{D_L}$. Vo=30 m.s^{-1}

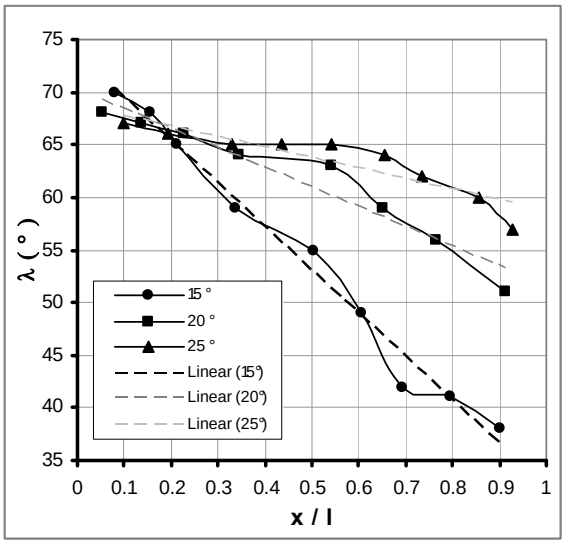

Fig. 17 Angular deviation λ, versus the reduced distance from P, x/l, for slant angles θ = 15, 20 and 25°. Vo=30 m.s^{-1}

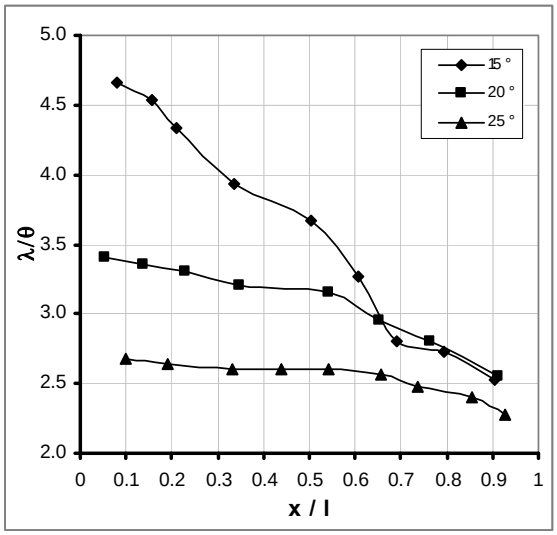

Fig. 18 Ratio between the angular deviation and the slant angle versus the reduced distance from P, x/l, for slant angles θ = 15, 20 and 25°. Vo=30 m.s^{-1}

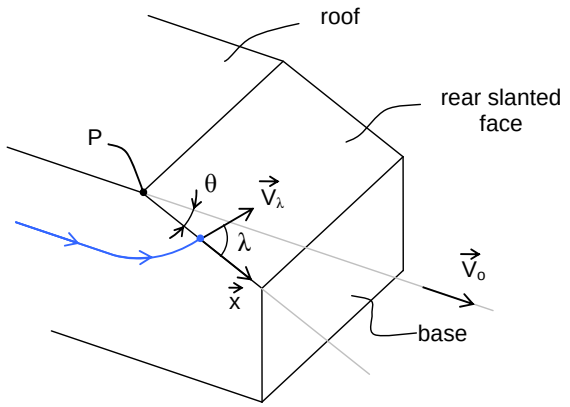

Fig. 19a Slant angle and angular deviation of the lateral friction line λ

Fig. 19b Friction line visualisations on the side of the rear window. θ = 15°, Vo=30 m.s^{-1}

Fig. 19c Friction line visualisations on the side of the rear window. θ = 20°, Vo=30 m.s^{-1}

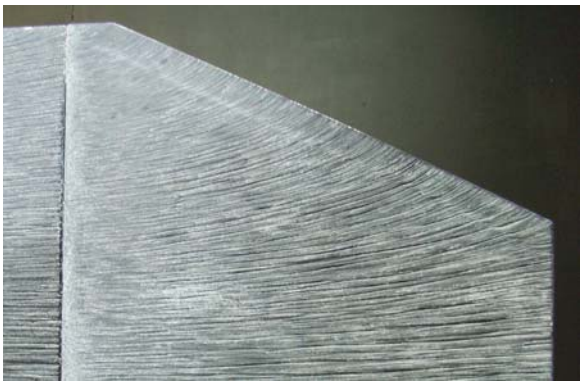

Fig. 19d Friction line visualisations on the side of the rear window. θ = 25°, Vo=30 m.s^{-1}

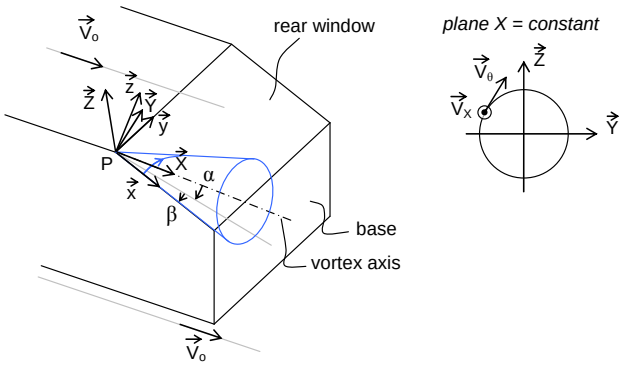

Fig. 20 Referential system linked to the swirling structure: Precession and nutation angles. Azimuthal V_θ and longitudinal V_X velocities in a X=Cte plane

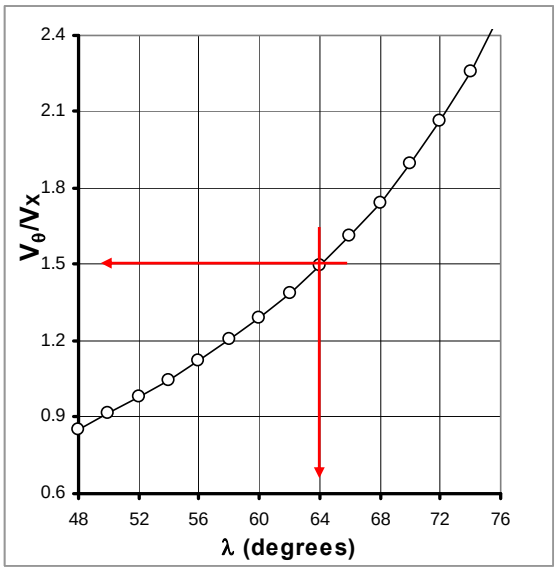

Fig. 21 Evolution of the ratio of azimuthal V_θ and longitudinal V_X velocities as a function of the deviation angle λ